Radio wave scattering by circumgalactic cool gas clumps

H. K. Vedantham[1,2⋆] and E. S. Phinney[1]

[1]*Cahill center for astronomy and astrophysics, California Institute of Technology, 1200 E. California Blvd. Pasadena, CA 91125, USA.*
[2]*Netherlands Institute for Radio Astronomy (ASTRON), Oude Hogeveensedijk 4, 7991 PD, Dwingeloo, Netherlands*

ABSTRACT

We consider the effects of radio-wave scattering by cool ionized clumps ($T \sim 10^4$ K) in circumgalactic media (CGM). The existence of such clumps are inferred from intervening quasar absorption systems, but have long been something of a theoretical mystery. We consider the implications for compact radio sources of the 'fog-like' two-phase model of the circumgalactic medium recently proposed by McCourt et al. (2018). In this model, the CGM consists of a diffuse coronal gas ($T \gtrsim 10^6$ K) in pressure equilibrium with numerous $\lesssim 1$ pc scale cool clumps or 'cloudlets' formed by shattering in a cooling instability. The areal filling factor of the cloudlets is expected to exceed unity in $\gtrsim 10^{11.5}\,M_\odot$ haloes, and the ensuing radio-wave scattering is akin to that caused by turbulence in the Galactic warm ionized medium (WIM). If 30 per-cent of cosmic baryons are in the CGM, we show that for a cool-gas volume fraction of $f_\mathrm{v} \sim 10^{-3}$, sources at $z_\mathrm{s} \sim 1$ suffer angular broadening by $\sim 15\,\mu$as and temporal broadening by ~ 1 ms at $\lambda = 30$ cm, due to scattering by the clumps in intervening CGM. The former prediction will be difficult to test (the angular broadening will suppress Galactic scintillation only for $< 10\,\mu$Jy compact synchrotron sources). However the latter prediction, of temporal broadening of localized fast radio bursts, can constrain the size and mass fraction of cool ionized gas clumps as function of halo mass and redshift, and thus provides a test of the model proposed by McCourt et al. (2018).

Key words: galaxies: haloes – scattering – radio continuum: transients

1 INTRODUCTION

The circumgalactic medium (CGM) of galaxies and the intergalactic medium (IGM) are together expected to harbour about 80 % all baryons in the Universe (Anderson & Bregman 2010). Absorption spectroscopy of quasars along intervening CGM sight-lines in recent years have yielded a wealth of information on the physical state of CGM gas. Some of these findings have however contradicted naive models based on theoretical considerations. In particular, the ubiquitous detection of cool ($\sim 10^4$ K) and likely dense ($n_e \sim 1\,\mathrm{cm}^{-3}$ at $z \approx 2$; Hennawi et al. 2015; Lau et al. 2016) gas in the CGM of massive galaxies ($M \gtrsim 10^{12}\,M_\odot$) is puzzling— an outcome that was not predicted by canonical galaxy assembly models. Based on theoretical consideration and numerical simulations, McCourt et al. (2018); Ji et al. (2017) have shown that numerous sub-parsec scale cool[1] gas clumps can form in

galaxy haloes due to thermal instabilities, likening the CGM to a 'fog' consisting of partially ionized $\sim 10^4$ K cloudlets dispersed in a hot $\sim 10^6$ K ambient medium. Such small clumps, though they can explain many features of quasar absorption lines, are however subject to uncertainly regarding the initial conditions, and destruction by electron conduction from the surrounding hot gas unless magnetically shielded. It therefore is desirable to have an observational probe capable of detecting the existence of such small clumps in the CGM of distant galaxies. Here we show that the fog-like CGM leads to observable scattering of radio waves from extragalactic sources, and that upcoming surveys for Fast Radio Bursts (FRB) can constrain the sub-parsec scale morphology of cool gas in intervening CGM.

The assembly of dissipative baryons into galaxies in the presence of dark matter potential wells has been studied extensively based on general physical principles(see e.g.

⋆ E-mail: vedantham@astron.nl
[1] The clumps of interest are photoionized gas at $\sim 10^4$K. In the recent CGM literature, whose terminology is used by McCourt et al, such clouds are called "cold", while gas at 10^{4-5}K is called "cool", and gas at 10^{5-6}K called "warm", in contrast to the volume-filling "hot" gas at $\sim 10^6$K. This is unfortunately

inconsistent with many decades of tradition of literature on the interstellar medium, in which partially ionized gas at 8000K is called "warm", while "cold" is reserved for neutral and molecular gas at much lower temperatures. To avoid confusion, in this paper we decided to call the photoionized clumps "cool" rather than "cold" or "warm".

Binney 1977; Silk 1977; Rees & Ostriker 1977; White & Rees 1978). The conclusion of these early studies relevant for this paper is as follows. Gravitational potential energy of baryons is converted to kinetic energy during dissipative collapse. This heats the baryons to the virial temperature $T_{\mathrm{vir}} \approx 10^6 \, M_{12}^{2/3} h^{2/3}(z) \, \mathrm{K}$, where M_{12} is the halo mass in units of $10^{12} \, M_\odot$ and $h(z)$ is the dimensionless Hubble parameter at redshift z of the halo. For haloes less massive than about $10^{11.5} \, M_\odot$, the virial temperature drops below $\sim 10^5 \, \mathrm{K}$, whereupon the radiative cooling timescale, t_{cool} (primarily via metal lines) is smaller than the Hubble time, t_0. The gas then rapidly cools to $T \sim 10^4 \, \mathrm{K}$ throughout the halo, loses pressure support, and falls inwards to form stars. In more massive haloes, $t_{\mathrm{cool}} \gg t_0$ and the gas at large radii $r \sim r_{\mathrm{vir}}$ forms a long-lived pressure-supported hot ($T \gtrsim 10^{5.5} \, \mathrm{K}$) halo devoid of cold neutral gas.[2]

Quasar absorption spectroscopy and fluorescent Lyα studies of the CGM, however, tell a somewhat different story. Absorption studies routinely detected large amounts ($N \sim 10^{18} - 10^{20} \, \mathrm{cm}^{-2}$) of cool $10^4 \, \mathrm{K}$ gas at the virial radius of $\gtrsim 10^{12} \, M_\odot$ haloes at both high ($z \sim 2$) and low ($z \sim 0$) redshifts (Steidel et al. 1988, 1994; Lau et al. 2016; Stocke et al. 2013; Werk et al. 2014; Mathes et al. 2017; Tumlinson et al. 2017). Studies of galaxies at redshifts $z \sim 0.1 - 2.5$ have shown that associated absorption lines are almost always found in the spectra of background quasars projected within 50–100 kpc of the galaxies(Tumlinson et al. 2017; Rudie et al 2012; Turner et al. 2014). Thus the covering factor of cool gas in galaxy halos exceeds 50% even at such large distances from the galaxies. Photoionization models, though uncertain, indicate that the projected mass surface density scales roughly as r^{-1} (Tumlinson et al. 2017, see e.g., Fig 7 of). Florescent Lyα imaging of quasar host galaxies at $z \sim 3$ provides additional cofirmation that cool gas has a covering fraction of unity even out to the virial radius, with a surface brightness that evolves with radius as $r^{-1.8}$ (Cantalupo et al. 2014; Borisova et al. 2016). Both the emission and absorption observations point to the ubiquitous nature of cool, $\sim 10^4 \, \mathrm{K}$ gas in the CGM of $M \gtrsim 10^{12} \, M_\odot$ halos— a result not predicted by the canonical model of halo formation. The radial profile and smooth absorption lines over the viral velocity width in addition disfavour any model where the cool gas is confined to a narrow shell around the virial shock, but instead suggests that the cool gas pervades the CGM in multiple small clouds with a total areal covering factor exceeding unity.

Broadly speaking, two classes of models have been advanced via sophisticated simulations to explain the large covering fraction of cool gas in massive galactic haloes. (a) The first set of models create the cool gas in-situ by recognizing that in practice, only a part of the accreted gas is likely heated to the virial temperature at the accretion shock (see e.g. Kereš et al. 2005, fig. 7) and/or by enhancing thermal instability via magnetic suppression of buoyant oscillation (Ji et al. 2017). The cooler ($T \lesssim 10^{5.5}$) gas can therefore cool well within t_0 *in situ*. (b) The second set of models transport the cool gas from near the galactic disk into the halo in the form of galactic winds (Faucher-Giguère et al.

---

[2] At some sufficiently small radius $r \ll r_{\mathrm{vir}}$, $t_{\mathrm{cool}} < t_0$ and the gas can collapse into stars.

2016). At present, these are somewhat heuristic arguments and the precise details of how cool gas is produced and sustained in galactic haloes remains an active field of study (see Tumlinson et al. (2017) for a recent review).

Absorption spectroscopy (Steidel et al. 1988; Tumlinson et al. 2017, e.g.) measures the column density of cool gas. The volume density can only be inferred from photoionization modelling that is fraught with uncertainties. Yet the volume density of cool gas in CGM and its internal clumpy structure are critical to a determination of its physical state, formation mechanism, and eventual fate. Recently McCourt et al. (2018) have employed simulations and theoretical arguments to study the condensation of cool $T \approx 10^4 \, \mathrm{K}$ clumps from a background of hot $T \gtrsim 10^6 \, \mathrm{K}$ gas that leads to the development of the classical two-phase medium (Field 1965). They argue that, akin to fragmentation in the Jeans' instability (Jeans 1902) of gravitationally collapsing clouds with $\gamma < 4/3$, cooling of clouds whose size greatly exceeds $c_s t_{\mathrm{cool}}$ does not proceed isochorically, but leads to continual fragmentation of gas into pieces of size $\sim c_s t_{\mathrm{cool}}$ which are able to maintain isobaric cooling, down to a length-scale of order the minimum of $c_s(T) t_{\mathrm{cool}}(T)$ as a function of temperature T. For radiative cooling curves relevant to astrophysical plasma, this characteristic minimum scale of cool clumps occurs at $T \sim 10^4$ and is $\sim (0.1 \, \mathrm{pc}) \, (n/\mathrm{cm}^{-3})^{-1}$. This predicts a fixed gas column density of the individual smallest clumps (independent of ambient pressure) of $N_e \approx 10^{17} \, \mathrm{cm}^{-2}$ (McCourt et al. 2018, their §2.1). Such small length-scales are currently well beyond the reach of halo-scale simulations and much smaller than can be constrained by photoionization modelling of absorption spectra.

By contrast, the scattering of radio waves is a highly sensitive function of small-scale density inhomogeneities. For instance, radio wave propagation through the Galactic warm ionized medium (WIM) has been used to study its density structure on spatial scales of $10^8 - 10^{15} \, \mathrm{cm}$ (Armstrong et al. 1995). Here we show that the same techniques can be applied to probe the structure of cool gas in the CGM. More importantly, the recent discovery of Fast Radio Bursts (FRB; Lorimer et al. 2007)— milli-second duration radio pulses originating at cosmic distances, opens up an unprecedented opportunity to revolutionize our understanding of the CGM, much in the same way the discovery of pulsars led to a profoundly improved understanding of the Galactic interstellar medium (Rickett 1990).

The rest of the paper is organized as follows. In §2, we lay down the basic halo properties as as function of mass and redshift. In §3 we compute the scattering characteristic of such haloes. In §4, we present a discussion of our results by considering the observable signature of scattering by the CGM of an ensemble of haloes in the Universe. We adopt the *Planck* cosmological parameters (Planck Collaboration et al. 2016): $H_0 = 67.8 \, \mathrm{km \, s^{-1} \, Mpc^{-1}}$, $\Omega_{\mathrm{m}} = 0.308$ and $\Omega_\Lambda = 1 - \Omega_{\mathrm{m}}$ throughout this paper. A glossary of symbols and their meaning is given in the Appendix for quick reference.

2   HALO PROPERTIES

We assume the usual definition of virial radius, r_{200} as the radius at which the matter density equals 200 times the critical density at any given redshift. The halo mass,

$M_{12} = M/10^{12}\,M\odot$ is then the mass enclosed within r_{200}:

$$r_{200} = \left(\frac{3M}{800\pi\rho(z)}\right)^{1/3} \approx 163\,M_{12}^{1/3}\,h^{-2/3}(z)\,\text{kpc}, \qquad (1)$$

where the critical density $\rho(z)$ is given by

$$\rho(z) = \frac{3H(z)^2}{8\pi G} \approx 277.34\,h^2(z)\,M\odot\,\text{kpc}^{-3}. \qquad (2)$$

Here $H(z)$ is the Hubble parameter at redshift z:

$$H(z) = H_0\sqrt{\Omega_{\text{m}}(1+z)^3 + \Omega_\Lambda}, \qquad (3)$$

and $h(z)$ is the dimensionless Hubble parameter defined as $H(z) = h(z) \times 100\,\text{km s}^{-1}\,\text{Mpc}^{-1}$. With the dark matter halo properties completely specified by equations 1 through to 3, we turn our attention to the gas properties.

2.1 Gas density

We assume that in the halo mass-range of interest, the infalling gas is shock heated to the virial temperature of

$$T_{\text{vir}} = 9.3 \times 10^5\,M_{12}^{2/3}h^{2/3}(z)\,\text{K}, \qquad (4)$$

The hot gas pressure at r_{200} and its profile is somewhat difficult to derive from first principles. We therefore pick a gas pressure at r_{200} that yields a predefined baryon fraction in the hot phase. There is currently no consensus on how the cosmic baryons are apportioned to the various gas and stellar phases. Current best constraints places about $20\,\text{per-cent}$ of baryons in galaxies (stars, gas and dust; see e.g. Anderson & Bregman 2010), while the remaining $80\,\text{per-cent}$ must be in the CGM and IGM (Tumlinson et al. 2017). We will normalize our results to the nominal case where $f_{\text{CGM}} = 30\,\text{per-cent}$ of baryons are in the CGM. We further assume a density profile of $n(r) \propto r^{-\alpha}$ for $0 < r \le r_{\text{shock}} = 1.5r_{200}$ with $\alpha = 1.5$ (Fielding et al. 2017). This yields a gas pressure at r_{200} of

$$P_{200}(M,z) = 27\left(\frac{f_{\text{CGM}}}{0.3}\right)M_{12}^{2/3}\,h(z)^{8/3}\,\text{cm}^{-3}\,\text{K}. \qquad (5)$$

2.2 Volume fraction and covering factor

The closest analog to the cool clumps that have been studied in any detail are the Milky Way's high velocity clouds (HVC). HVCs detected in emission have a total mass of about $2.6\times10^7\,M\odot$ (Putman et al. 2012) which yields a lower limit on cool gas volume fraction of about $f_{\text{v}} > 10^{-5}$. Several authors have studies absorption line systems at higher redshifts up to $z \sim 2$. The measured column densities in conjunction with photo-ionization modeling yield volume fractions of $f_{\text{v}} = 10^{-4} - 10^{-3.5}$ (Lau et al. 2016; Hennawi et al. 2015; Prochaska & Hennawi 2009; Stocke et al. 2013). We refer the reader to McCourt et al. (2018, their Table 1) for a summary of these results. Photo-ionization modeling sufferers from considerable uncertainties. In limited cases, fine structure lines may be used to get a direct estimate of gas densities without the need for photo-ionization modeling. Such observations also show large gas densitiesLau et al. (2016) in excess of $\sim 1\,\text{cm}^{-3}$ that imply comparable volume filling fractions. Hence, we will adopt a characteristic of $f_{\text{v}} = 10^{-4}$ when a specific number is required, but we will carry f_{v} as a variable in our equations such that variations between photo-ionization models may be included in the future.

There is sparse observational constraint regarding the radial evolution of the volume fraction. Borisova et al. (2016) find that the surface brightness of the Lyα fluorescent emission in $z \sim 2 - 3$ CGM has a power-law variation, $r^{-1.8}$. If the volume density of cool gas evolves as $r^{-1.5}$ as seen in simulations (Fielding et al. 2017), then the fluorescent emission can be reconciled with a volume fraction that changes only weakly with radius as $f_{\text{v}}(r) \propto r^{-\beta}$, with $\beta = -0.2$. We will adopt this value throughout.

The foggy-CGM model under consideration here specifically addresses the large areal covering factor of cool gas despite its low volume fraction as implied by photo-ionization modeling. The number of cool clumps encountered by a sightline at a characteristic impact factor of b is given by $f_{\text{a}}(b) \approx f_{\text{v}}(b)\,b/r_{\text{c}}$ where r_{c} is the radius of the individual cloudlets that comprise the CGM fog. Because the column density in individual cloudlets is fixed by the model under consideration at $N_e = 10^{17}\,\text{cm}^{-2}$, the cloudlet size at radius r is $r_{\text{c}}(r) = 0.5N_e/n_e(r)$ which gives

$$f_{\text{a}}(b) \approx 3\left(\frac{f_{\text{CGM}}}{0.3}\right)\left(\frac{f_{\text{v}}}{10^{-4}}\right)M_{12}h^2(z)\left(\frac{b}{r_{200}}\right)^{1-\beta-\alpha} \qquad (6)$$

For our fiducial values of $\alpha = 1.5$, $\beta = -0.2$, $f_{\text{v}} = 10^{-4}$, $f_{\text{CGM}} = 0.3$, the covering fraction of cloudlets exceeds unity at impact parameter $b \sim r_{200}$ for haloes above $10^{11.9}\,M\odot$ at $z = 0$ or above $10^{11.4}\,M\odot$ at $z = 1$. This fog-like nature of the CGM wherein a low volume fraction leads to a high areal covering factor is depicted in Fig. 1 with some characteristic parameter values for a $10^{12}\,M\odot$ halo at $z = 1$. The reader may readily scale the numbers to other halo masses and redshifts via equations 1 though 6. The resulting densities and high areal covering factors are roughly consistent with inferences from observations of quasar absorption systems: see for instance McCourt et al. (2018, their Table. 1), who present a compilation of relevant observational inferences from (Stocke et al. 2013; Lau et al. 2016; Prochaska & Hennawi 2009; Hennawi et al. 2015).

2.3 Neutral fraction

The last aspect of haloes that needs specification is the ionization fraction, since only free electrons contribute to radio wave scattering. We adopt an intergalactic UV photoionization rate to be $\Gamma(\text{IGM}) = 10^{-13}\,[(1+z)/1.2]^5\,\text{sec}^{-1}$ (Gaikwad et al. 2017) to determine the neutral fraction at different radii, $\zeta(r)$. Details of our photoionization-equilibrium calculations in a fog-like CGM is is given in the Appendix. We find that individual cloudlets with their column density of $10^{17}\,\text{cm}^{-2}$ are only partially ionized, but the fog can self-shield itself against the extragalactic radiation field below a critical radius that, for $\alpha = 1.5$, $\beta = -0.2$, has an approximate value of (proof in Appendix)

$$r_{\text{ss}} \approx 0.11\left(\frac{f_{\text{v}}}{10^{-4}}\right)^{0.56}\left(\frac{f_{\text{CGM}}}{0.3}\right)^{1.11}M_{12}^{0.93}\frac{h^{2.59}(z)}{(1+z)^{2.78}}. \qquad (7)$$

At radii below r_{ss} the clouds rapidly achieve neutrality. We therefore find that haloes more massive that $10^{13.2}\,M\odot$ at $z = 0$ or $10^{13.4}\,M\odot$ at $z = 1$ can self shield themselves even at their virial radius. The halo mass range that is relevant for radio wave scattering is therefore bounded. On the lower mass end, haloes less massive than $10^{11.5}\,M\odot$ are not expected to have long-lived pressure supported halo gas, and
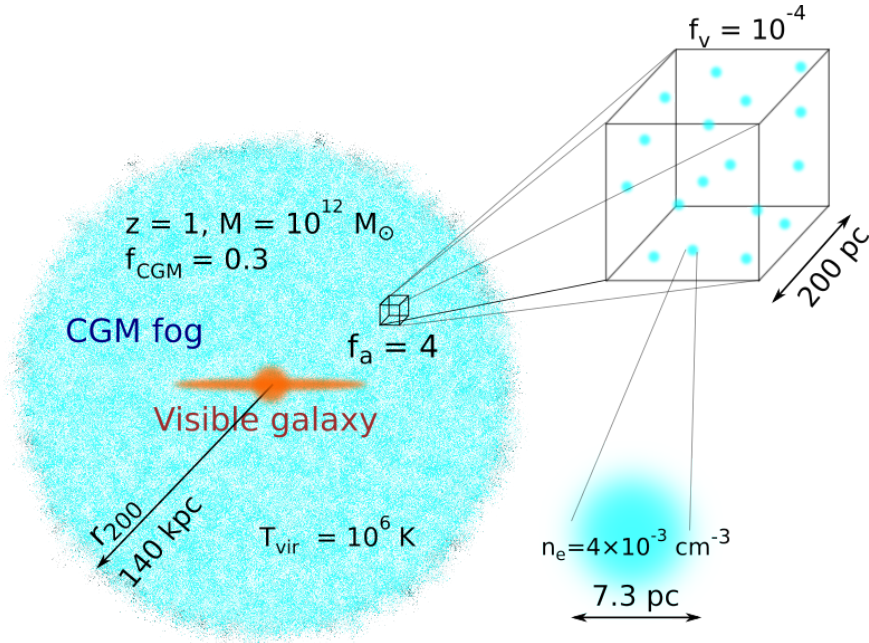
Figure 1. A depiction of the fog-like CGM model considered here and some characteristics physical parameters for a $10^{12}\,M_\odot$ halo at $z = 1$. Cyan denotes the cool 10^4 K gas clumps or 'cloudlets' that are dispersed in a virial-shock heated 10^6 K halo gas. The cloudlets have a large areal covering factor despite their small volume fraction.
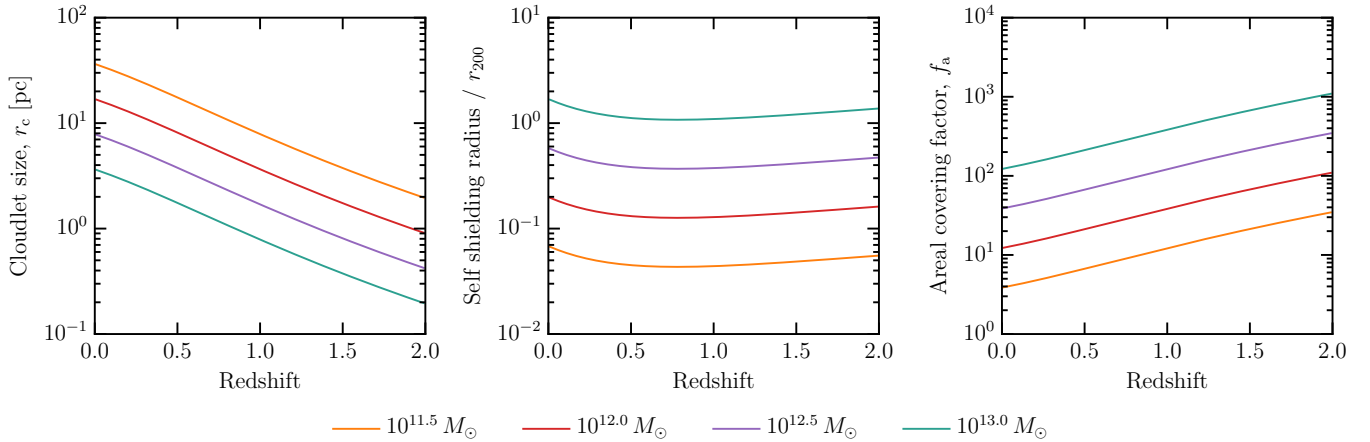
Figure 2. CGM fog characteristics assumed in this paper (equations 1 to 6). The column density through individual cloudlets and the cloudlet volume fraction are taken to be $N_e = 10^{17}\,\mathrm{cm}^{-2}$, and $f_v = 10^{-4}$ respectively. The cloudlet size, r_c and the areal covering factor, f_a are evaluated at the viral radius, r_{200}, and evolve with radius according $r^{1.5}$ and $r^{0.2}$ respectively

haloes more massive than about $10^{13.5}\,M_\odot$ can self shield themselves against ionization from the extragalactic radiation field. Now that the halo mass range and the relevant gas properties have been specified, we turn our attention to the problem of computing the scattering parameters.

3   SCATTERING BY A SINGLE HALO

Before considering the scattering of radio waves from a cosmic distribution of haloes, it is instructive to built up our analysis starting with the scattering properties of a single cool gas clump, which we will call as a 'cloudlet' after Mc-Court et al. (2018).

3.1   Dispersion in a cloudlet

Propagation through plasma of column density N_e advances the phase of a monochromatic wave of wavelength λ by $\phi = \lambda N_e r_e$ where r_e is the classical electron radius. Wave diffraction is a result of fluctuations of phase ϕ transverse to the direction of propagation. Specifically, a transverse gradient of $\partial\phi/\partial r$ leads to a deflection of the direction of light propagation through an angle (geometry sketched in Fig. 3)

$$\theta_{\rm sc} = \frac{\lambda}{2\pi}\frac{\partial\phi}{\partial r} \tag{8}$$
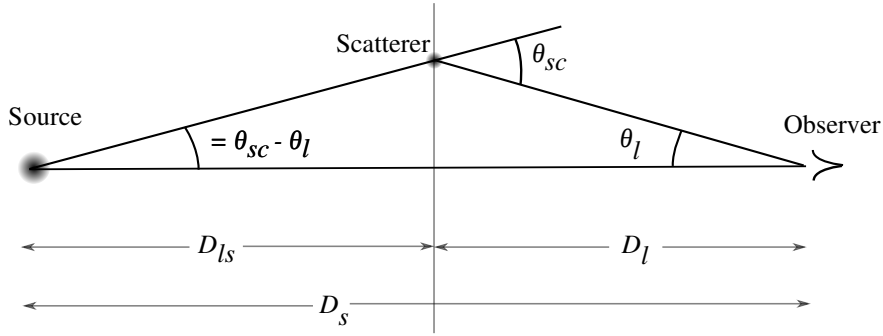
Figure 3. A not to scale sketch of the scattering geometry and symbols used in this paper.

For a cloudlet radius of r_c, the phase gradient is $\partial\phi/\partial r \sim \lambda N_e r_e/r_c$, which gives a characteristic deflection angle of

$$\theta_{sc} \sim 0.3\,\mu\text{as}\ \lambda_{30}^2\, N_{e,17}\, (r_c/1\,\text{pc})^{-1} \qquad (9)$$

The geometric delay between the time of arrival of signals from multiple images may also be observed in impulsive sources such as fast radio bursts. Here again, the cosmological distances will have profound effect. The characteristic time delay is

$$\Delta\tau \approx \frac{\theta_{sc}^2}{2c}\frac{D_{ls}D_l}{D_s} \qquad (10)$$

The delay is maximized for a geometry where $D_{ls} = D_l$:

$$\Delta\tau_{\text{max}} \approx 0.05\,\mu\text{s}\ (D_l/1\,\text{Gpc})\,\lambda_{30}^4\,N_{e,17}^2\,(r_c/1\,\text{pc})^{-2} \qquad (11)$$

which is comparable to the temporal broadening due to scattering in the Galactic WIM towards Pulsars at high Galactic latitude (see for e.g. Manchester et al. 2005). We therefore conclude that even an isolated cloudlet at cosmological distances leads to measurable effects on radio waves. Because we expect typical sight-lines through the CGM to intercept a large number of cloudlets (equation 6), we now generalize these results to the case of a random cloudlet ensemble.

3.2 Ensemble scattering properties

The volume filling fraction of cloudlets is expected to be small: $\sim 10^{-4}$, and we treat the cloudlets as discrete objects that are randomly distributed. The transverse phase gradient imparted by such an ensemble of cloudlets is a random variable, whose statistical properties are best expressed in terms of the phase structure function, $D_\phi(\Delta r)$ defined as:

$$D_\phi(\Delta r) \equiv \langle [\phi(r) - \phi(r + \Delta r)]^2 \rangle \qquad (12)$$

where the angular brackets denote ensemble average, and $\phi(r)$ is the total wave phase at transverse co-ordinate r. The structure function therefore measures the variance of phase differences between two sight-lines that separated by a transverse distance Δr, and is the statistical analogue of the transverse phase gradient $\partial\phi/\partial r$ used in §2.2 to compute the scattering angle.

If there be on average f_a cloudlets intercepted by a sight-line, the structure function can be shown to be (see Appendix)

$$D_\phi(\Delta r) = 2\lambda^2 r_e^2 N_e^2 f_a \Psi(\Delta r/r_c), \qquad (13)$$

where the function $\Psi(.) \leq 1$ only depends on the internal
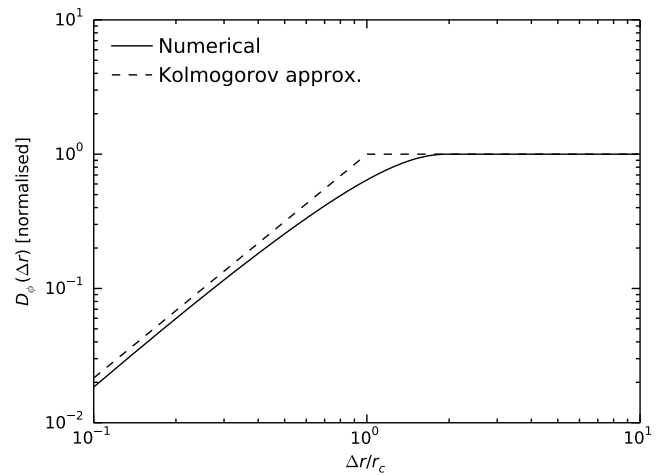
Figure 4. The normalize phase structure function of an ensemble of spherical cloudlets with uniform density, compared to a Kolmogorov structure function with the same normalization and an outer-scale of r_c. The structure function is normalized by the factor $2f_a (\lambda r_e N_e)^2$.

structure of the cloudlets and determines the slope of the phase structure function.

The upper panel of Fig. 4 shows the numerically computed, normalized structure function $\Psi(\Delta r/r_c)$ for a spherical cloudlet. As anticipated, the differential phase increases monotonically for $\Delta r < r_c$. Beyond a transverse separation of r_c, rays encounter an independent realization of cloudlets and the structure function saturates and becomes independent of Δr. The saturated value of the structure function is simply the Poisson variance in the phase accumulated along two independent realization of the cloudlet ensemble which is $2f_a \times (\lambda r_e N_e)^2$. Here the first term is the Poisson variance in the differential number of cloudlets on two independent sight-lines and the second terms if the square of the radio-wave phase through a single cloudlet.

The bottom panel of Fig. 4 shows the logarithmic slope of the structure function under the spherical cloudlet assumption. The slope is less than the critical value of 2, which implies a 'shallow spectrum' in which the transverse phase structure on smaller spatial scales dominate the scattering as opposed to larger scales fluctuations (Goodman & Narayan 1985). At smaller spatial scales ($\Delta r \ll r_c$), the slope is close to the Kolmogorov value of 5/3, which is usually employed

to model wave scattering in extended turbulent media. We will therefore proceed with the assumption that the structure function is 'Kolmogorov-like' with an outer scale of r_c and total phase variance of $2\lambda^2 N_e^2 r_e^2 f_a$:

$$D_\phi(\Delta r) = \left(\frac{\Delta r}{r_{\rm diff}}\right)^{5/3} \quad \Delta r < r_c$$
$$2\lambda^2 N_e^2 r_e^2 f_a \quad \text{otherwise} \qquad (14)$$

where, the diffractive scale $r_{\rm diff}$ is

$$r_{\rm diff} = r_c \left(2\lambda^2 N_e^2 r_e^2 f_a\right)^{-3/5}, \qquad (15)$$

or

$$r_{\rm diff} \sim 1.6 \times 10^{10} \,{\rm cm}\ (r_c/1\,{\rm pc})\ \lambda_{30}^{-6/5}\ N_{e,17}^{-6/5}\ (f_a/10)^{-3/5} \quad (16)$$

For comparison, the Galactic WIM has a diffractive scale of $\sim 10^{9.5}\,{\rm cm}$ at $\lambda = 30\,{\rm cm}$ (Armstrong et al. 1995, their fig. 2). Hence we expect the cloudlet ensemble to scatter incoming light through angles that are comparable to that from the Galactic WIM.

The typical scattering angle can be computed analogous to equation 8, by noting that the stochastic phase fluctuates by $\sim 1\,{\rm rad}$ over a transverse extent equal to the diffractive scale. This gives $\partial\phi/\partial r \sim 1/r_{\rm diff}$, and the characteristic scattering angle becomes

$$\theta_{\rm sc} = \frac{\lambda}{2\pi r_{\rm diff}}, \qquad (17)$$

or

$$\theta_{\rm sc} \sim 63\,\mu{\rm as}\ (r_c/1\,{\rm pc})^{-1}\ \lambda_{30}^{11/5}\ N_{e,17}^{6/5}\ (f_a/10)^{3/5} \quad (18)$$

The characteristic temporal broadening (equation 10) is much larger than that seen in the Galactic WIM:

$$\Delta\tau \sim 0.4\,{\rm ms}\ (r_c/1\,{\rm pc})^{-2}\ \lambda_{30}^{22/5}\ N_{e,17}^{12/5}\ (f_a/10)^{6/5}$$
$$\times \left(\frac{D_{ls}D_l/D_s}{1\,{\rm Gpc}}\right). \qquad (19)$$

3.3 Dependence on halo mass and impact parameter

Lets us now evaluate the scattering angle and temporal broadening when the sight-line passes a halo of a given mass at some redshift with an impact parameter b. Such a ray will pass through cloudlets at varying radii which will possess varying scattering strengths. Ideally one would evaluate the integral $\int dy\, \partial D_\phi(\Delta r, y)/\partial y$ along the ray-path within the halo with y as the affine parameter. However, scattering is dominated by the densest[3] part of the halo along the ray path. We can therefore obtain reasonably accurate values for the scattering parameters by assuming that a ray with impact parameter b traverses a distance of b along a cloudlet ensemble with volume filling factor $f_v(b)$ and cloudlet radius of $r_c(b)$. The areal covering factor along such a ray is $f_a(b) = f_v(b)\,b/r_c$. Following a proceeder similar to that in §3.2, we obtain an expression for the diffractive scale at impact parameter b:

$$r_{\rm diff}(b_{200}) = \left(2\lambda^2 N_e^2 r_e^2\right)^{-3/5}\ [r_c(b)]^{8/5}\ [f_v(b)b]^{-3/5}. \qquad (20)$$

[3] By densest, we imply largest f_v and smallest r_c.

Substituting $r_c(b) = N_e T/[2P(b)]$ and employing the halo properties from §2, we get

$$\frac{r_{\rm diff}(b)}{10^{11}\,{\rm cm}} = 3.5 \left(\frac{\lambda_{30}}{1+z}\right)^{-1.2} \left(\frac{f_v}{10^{-4}}\right)^{-0.6} \left(\frac{f_{\rm CGM}}{0.3}\right)^{-1.6}$$
$$\times M_{12}^{-1.27} h^{-3.87}(z) b_{200}^{1.68}$$
$$\text{for } r_{\rm shock} > b_{200} > 1.5 r_{\rm ss}, \qquad (21)$$
$$= 0.17 \lambda_{30}^{-1.2} \left(\frac{f_v}{10^{-4}}\right)^{0.34} \left(\frac{f_{\rm CGM}}{0.3}\right)^{0.27} M_{12}^{0.29}$$
$$\times h^{0.48}(z)\,(1+z)^{-3.47} \text{ for } b_{200} < 1.5 r_{\rm ss}, \quad (22)$$

where we have enforced the saturation of $r_{\rm diff}$ due to self-shielding. The saturation radius of $1.5 r_{\rm ss}$, instead of simply $r_{\rm ss}$ (see equation 7) was chosen to match $r_{\rm diff}$ versus b profiles obtained from full numerical integration of $\partial D_\phi(y)/\partial y$ along the ray path in the halo.

The corresponding scattering angle is

$$\frac{\theta_{\rm sc}(b)}{\mu{\rm as}} = 2.5 \left(\frac{\lambda_{30}}{1+z}\right)^{2.2} \left(\frac{f_v}{10^{-4}}\right)^{0.6} \left(\frac{f_{\rm CGM}}{0.3}\right)^{1.6} M_{12}^{1.27}$$
$$\times h^{3.87}(z) b_{200}^{-1.68} \text{ for } r_{\rm shock} > b_{200} > 1.5 r_{\rm ss},$$
$$= 50\ \lambda_{30}^{2.2} \left(\frac{f_v}{10^{-4}}\right)^{-0.34} \left(\frac{f_{\rm CGM}}{0.3}\right)^{-0.27} M_{12}^{-0.29}$$
$$\times h^{-0.48}(z)\,(1+z)^{2.47} \text{ for } b_{200} < 1.5 r_{\rm ss}. \quad (23)$$

The apprent size of the scattering disc is $\theta_{\rm ap} = \theta_{\rm sc} D_{ls}/D_s$. Finally, the temporal broadening timescale is

$$\frac{\Delta\tau}{\rm ms} = 7.6 \times 10^{-3} \left(\frac{\lambda_{30}}{1+z}\right)^{4.4} \left(\frac{f_v}{10^{-4}}\right)^{1.2} \left(\frac{f_{\rm CGM}}{0.3}\right)^{3.2}$$
$$\times M_{12}^{2.54} h^{7.74}(z) b_{200}^{-3.36} \left(\frac{D_{\rm eff}}{1\,{\rm Gpc}}\right)$$
$$\text{for } r_{\rm shock} > b_{200} > 1.5 r_{\rm ss},$$
$$= 3\ \lambda_{30}^{4.4} \left(\frac{f_v}{10^{-4}}\right)^{-0.68} \left(\frac{f_{\rm CGM}}{0.3}\right)^{-0.54} M_{12}^{-0.58}$$
$$\times h^{-0.96}(z)\,(1+z)^{4.94} \left(\frac{D_{\rm eff}}{1\,{\rm Gpc}}\right)$$
$$\text{for } b_{200} < 1.5 r_{\rm ss}. \qquad (24)$$

where the effective distance is $D_{\rm eff} = D_{ls}D_l/D_s$. With the above equations, we can now compute the optical depth to scattering for any halo mass function. Figure 5 shows a to-scale depiction of the scattering properties and projected sizes of haloes of various masses and redshifts. Figure 6 compares the analytical approximation to the scattering angle with the result of (a) numerically solving the equilibrium neutral fraction at each location in the halo and then (b) numerically integrating the phase structure function along the CGM sight-line. The agreement is good and we will use equation 21 to 24 to compute the statistics of scattering by a cosmic distribution of haloes in §4.

3.4 The impact of granularity

Before we extent the formalism to account for scattering from multiple halos, we pause to appreciate the impact of pc-scale cloudlet structure on CGM scattering. Consider a $10^{12}\,M_\odot$ halo at $z = 1$ with a cool-gas volume fraction of $f_v = 10^{-4}$, and a fraction $f_{\rm CGM} = 0.3$ of baryons in the CGM. The column density of the hot-phase gas would be
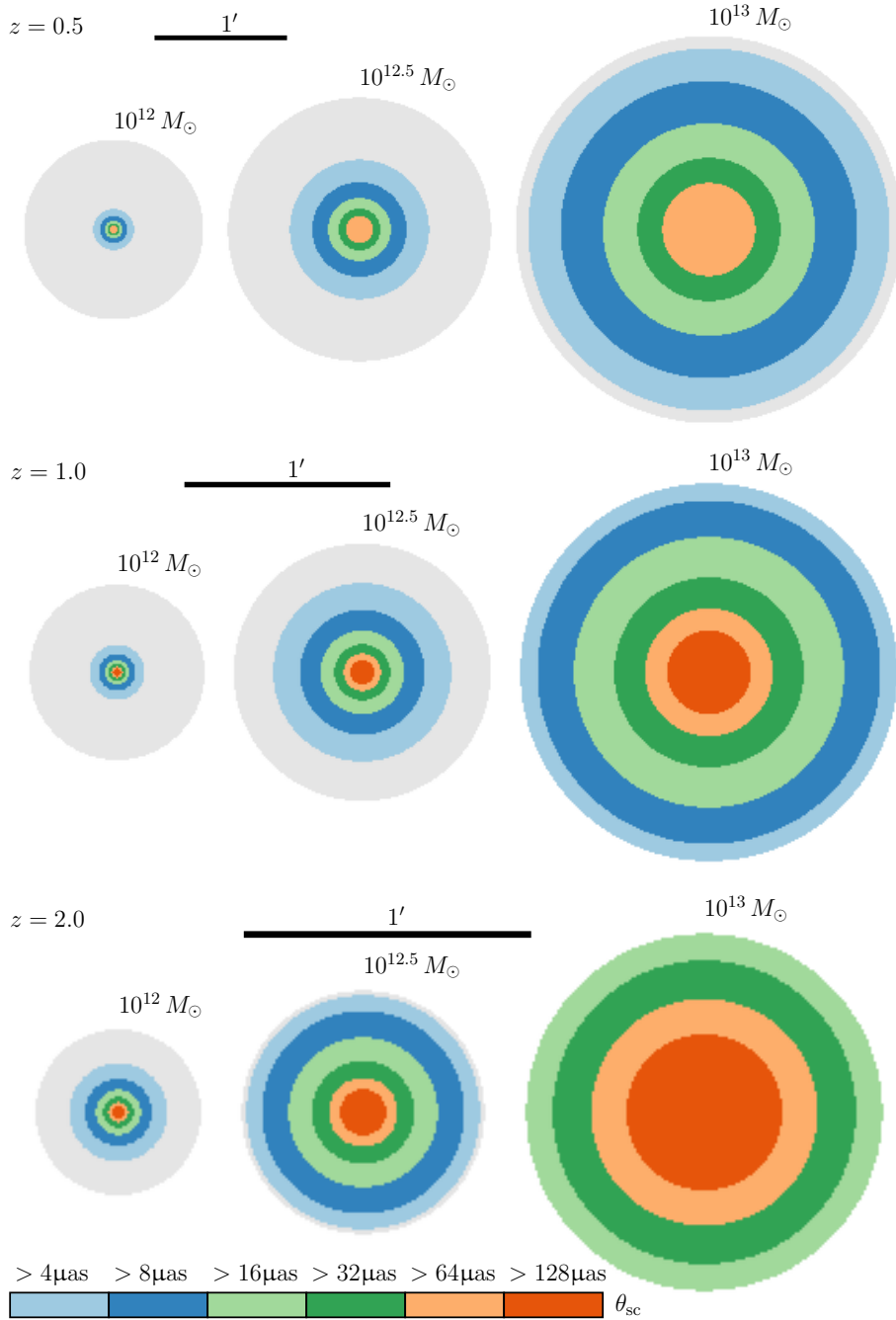
Figure 5. To-scale cartoons showing the relative amount of projected sky area within which the scattering angle exceeds the value given by the colour code, for haloes of varying mass (10^{12}, $10^{12.5}$ and $10^{13} M_\odot$). Each row corresponds to a different halo redshift. Scattering strength is parametrized as the characteristics ray deflection angle, $\theta_{\rm sc}$ at an observed wavelength of $\lambda = 30\,{\rm cm}$ (observed size of the scattering disc is $\theta_{\rm ap} = \theta_{\rm sc}\, D_{\rm ls}/D_{\rm s}$). The gray background marks the virial extent of the halo.

$N_e \approx 2 \times 10^{19}$. If this gas were fully turbulent with an outer scale of $r_{200} \approx 140\,{\rm kpc}$, then its diffractive scale at $\lambda = 30\,{\rm cm}$ is $r_{\rm diff} \approx 4 \times 10^{13}$ cm. The diffractive scale due to scattering by cloudlet in our formalism is $r_{\rm diff} \approx 2 \times 10^{11}$ cm— about two orders of magnitude smaller. Hence even though the cool gas only has a volume fraction of 10^{-4}, it scatters radio waves though a characteristic angle that is two orders of magnitude larger. This is a direct result of the small-scale granularity of cool gas in the cloudlet model considered here.

In other words, radio-wave scattering is highly sensitive to the small-scale fluctuations in gas density.

4 DISCUSSION AND SUMMARY

We will now discuss the observable impact of scattering in the CGM. To do so, we first predict the scattering properties of an ensemble of haloes.
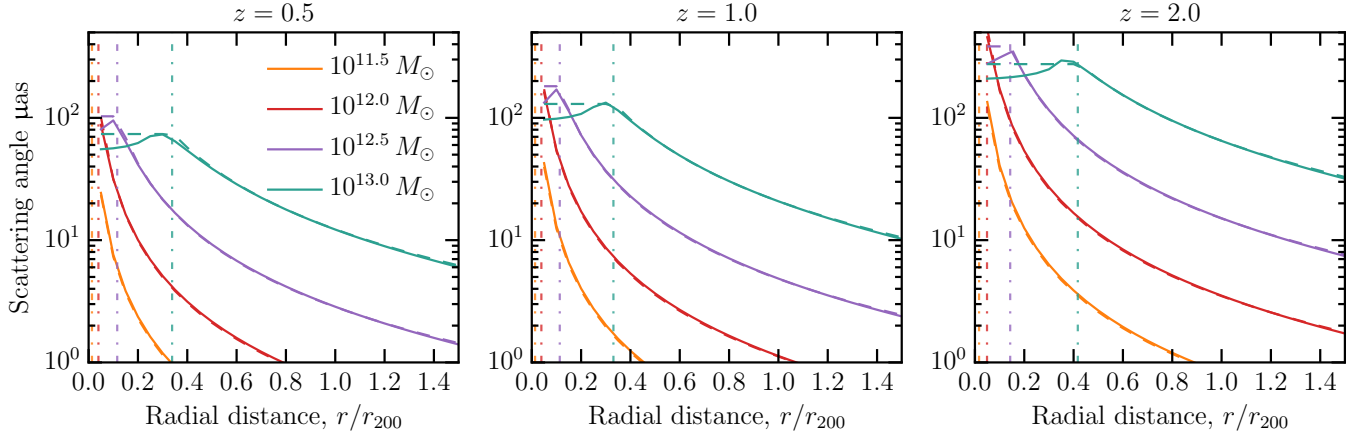
Figure 6. Solids lines: plots of scattering angle, θ_{sc} versus impact parameter, b_{200} (same data as in Fig. 5) for varying halo mass. Dashed lines: analytical approximation from equation 23. The vertical dot-dashed lines mark $1.5\,r_{ss}$ (defined in equation 7) where the scattering is expected to saturate due to self-shielding against the ionizing IGM background radiation.

4.1 Scattering in a ΛCDM Universe

We assume that the volume fraction of cool gas is redshift independent. The halo scattering properties however remain redshift dependent due to the evolution of virial pressure and halo number counts with redshift. We use the halo mass function calculator of Murray et al. (2013) to compute $dN(z,M)/dM$— the co-moving volume density of haloes of with mass in an infinitesimal interval dM about M, at redshift z. Fig. 7 shows the ensuing numbers of haloes larger than a mass shown in the legend, that are intercepted (within their virial shock) by an average sightline through the Universe. We find that nearly all sight-lines out to $z \sim 1$ pass within the virial radius of a $10^{13}\,M_\odot$ halo, and $\sim$ ten $10^{11}\,M_\odot$ halo. Because larger haloes (a) condense out of the Hubble flow at later times and (b) possess smaller virial radii at higher redshift, the number of intercepts for any given mass range rise up to $z \sim 1$ and decline thereafter.

Consider a radio source at redshift z_s. The statistics of the scattering timescales from all intervening haloes at redshift $z_l < z_s$ can be computed as follows. We pick a scattering timescale τ_{sc}, and for each halo mass and redshift bin, we compute the impact parameter $b_{\max}(M, z_l, z_s, \tau_{sc})$ below which the scattering timescale exceeds τ_{sc} via equation 24. The projected area is $\pi b_{\max}^2 / D_l^2$. There are $dN(M, z_l)/dM$ haloes per unit volume that contribute to the scattering. The areal covering factor of sightlines whose scattering timescale exceed τ_{sc} is therefore

$$\mathcal{A}(> \tau_{sc}) = \int d^2 V(z) \int_{M_{\min}}^{M_{\max}} dM \, \frac{dN(M, z_l)}{dM}$$
$$\times \frac{\pi b_{\max}^2(M, z_l, z_s, \tau_{sc})}{D_l^2} \quad (25)$$

where $M_{\min}$ and $M_{\max}$ are the mass range of interest, assumed to be $10^{11.5}\,M_\odot$ and $10^{13.5}\,M_\odot$ respectively, and $d^2 V(z)$ is the co-moving volume element at redshift z given by:

$$d^2 V(z) = c^3 \, \frac{\left(\int_0^z dz\prime / H(z\prime) \right)^2}{H(z)} \, dz \, d\Omega \quad (26)$$

We note that $\mathcal{A}(> \tau_{sc})$ can be larger than unity which
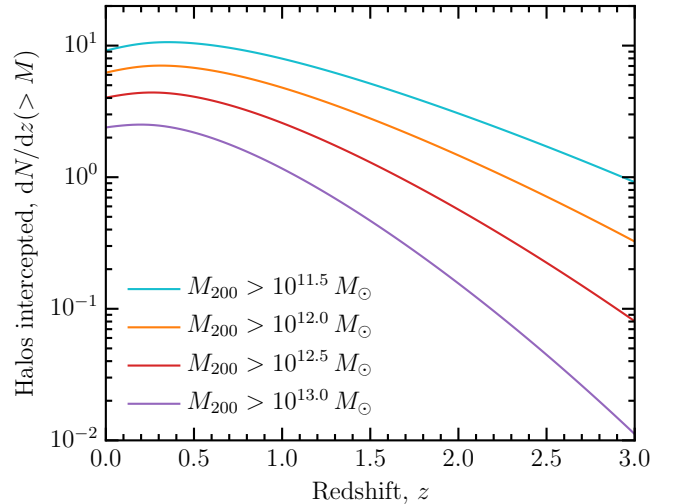
Figure 7. Number of virial intercepts by haloes with mass in excess of value shown in legend per unit redshift bin. Halo mass functions were computed using the program of Murray et al. (2013), and the footprint of each halo extended to a radius of $r_{\mathrm{shock}} = 1.5\,r_{200}$ (see eqn. 1).

indicates that there is more than one halo along the sight-line whose 'stand-alone' scattering strength exceeds τ_{sc}. An identical procedure can be followed for any other scattering parameter such as the apparent size of the scattering disc. Figure 8 shows the apparent angular size of the scattering disc and the scattering timescale calculated using the above prescription. The figure shows that most sight-lines out to $z_s = 1$ suffer angular broadening of at least $\sim 8\,\mu$as and temporal broadening of at least ~ 0.1 ms. The scattering for $z_s \gtrsim 0.2$ happens due to many intervening haloes. To understand their effect, we must compute the average scattering angle.

To first order, the scattering angle due to multiple scattering 'screens' add in quadrature, and the scattering timescale add linearly (Blandford & Narayan 1985, their Appendix A). We can therefore compute the mean scattering
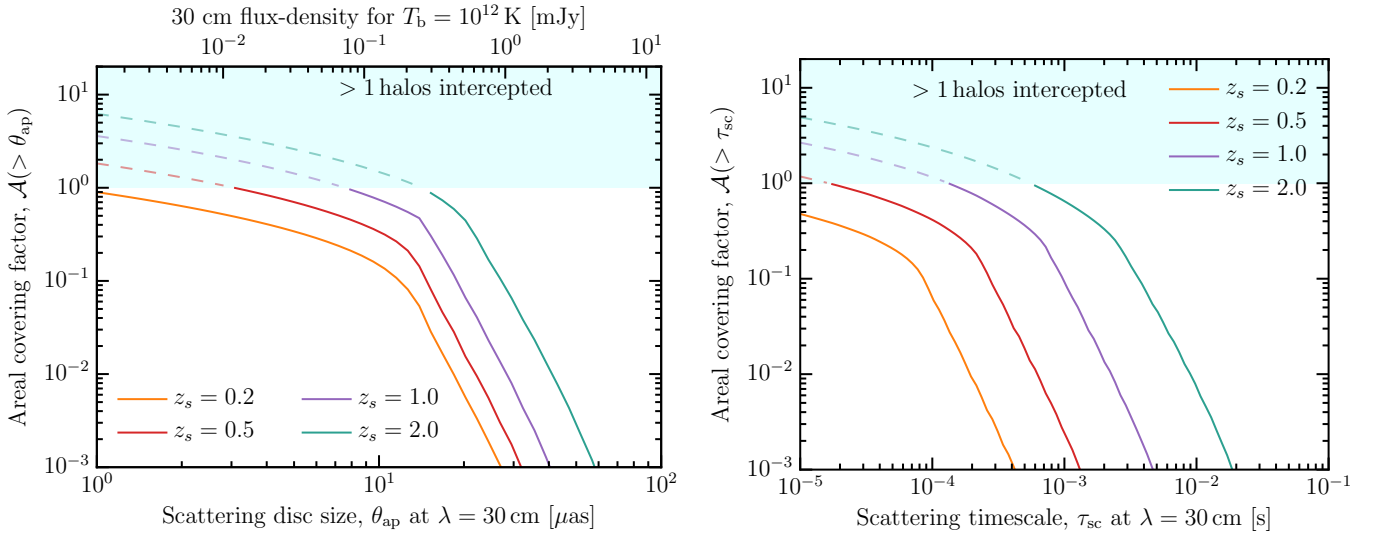
Figure 8. Left: Areal covering factor of sight-lines with scattering angle in excess of value on x-axis. Right: Same as left, but for scattering timescale. A covering factor > 1 implies there is more than one intervening halo whose scattering individually exceeds the x-axis value. Assumed parameter values are $f_{\rm v} = 10^{-4}$, $f_{\rm CGM} = 0.3$, $\Gamma = 10^{-13} \left[(1 + z_l)/1.2 \right]^5 \, {\rm s}^{-1}$

timescale as

$$\overline{\tau_{\rm sc}} = -\int_0^\infty {\rm d}\tau \, \tau \, \frac{{\rm d}\mathcal{A}(> \tau)}{{\rm d}\tau} \qquad (27)$$

where (the negative of) the differential in the integrand returns the probability density function of τ and the integral therefore evaluates to the expected value of τ. The mean size of the scattering disc is similarly

$$\overline{\theta_{\rm ap}} = \sqrt{-\int_0^\infty {\rm d}\theta \, \theta^2 \, \frac{{\rm d}\mathcal{A}(> \theta)}{{\rm d}\theta}} \qquad (28)$$

Figure 9 shows the mean temporal and angular broadening this computed as a function of source redshift for different values of cool-gas volume fraction $f_{\rm v}$ and fraction of baryons in the CGM, $f_{\rm CGM}$. The fractional sample variance on the mean is driven in large part by the Poisson fluctuations in the number of intercepted haloes. Based on Fig. 7, the fractional variation is of order unity for $z_{\rm s} \lesssim 0.2$ and reduces to few tens of per-cent by $z_{\rm s} \sim 1$. order unity for $z_{\rm s} \lesssim 0.2$ and decreases to tens of per-cent by $z_{\rm s} \sim 1$.

4.2 How can CGM scattering be observed?

Figure 9 shows that sources at $z_{\rm s} \gtrsim 1$ are scatter broadened to typical angular size of $\sim 20 \, \mu$as and in timescale to about $\gtrsim 1 \, {\rm ms}$, at a wavelength of $\lambda = 30 \, {\rm cm}$. Despite the considerable uncertainty in parameters affecting CGM scattering (specifically $f_{\rm v}$ and $f_{\rm CGM}$), let us take these numbers as a fiducial test case, to understand the observational manifestation of CGM scattering.

4.2.1 Refractive and diffractive scales

We first summarize the relevant aspects of two regimes of scattering: diffractive and refractive.[4] Diffractive effects

---

[4] Also called fast and slow scintillation respectively. See Rickett et al. (1984); Goodman & Narayan (1985) for further details.

Table 1. A comparison of characteristic angular and time-scales for scattering in the CGM (this work) and the Galactic warm ionized medium (Walker 1998). A refractive scale of $\theta_{\rm ap} = 20 \, \mu$as at $\lambda = 30 \, {\rm cm}$ has been assumed for the CGM contribution (see Fig. 8).

Parameter	CGM	MW (high lat.)
Transition wavelength ($\lambda_{\rm tran}$)	0.3 cm	3.75 cm
Length-scale	1 Gpc	1 kpc
Fresnel scale at $\lambda_{\rm tran}$	$10^{-3} \, \mu$as	3 μas
Diffractive angular scale ($\lambda = 30 \, {\rm cm}$)	$10^{-6} \, \mu$as	0.25 μas
Refractive angular scale ($\lambda = 30 \, {\rm cm}$)	20 μas	0.3 mas
Diffractive time scale ($\lambda = 30 \, {\rm cm}$)	5 min/0.5 s[†]	10 min
Refractive timescale[†] ($\lambda = 30 \, {\rm cm}$)	180 yr/0.3 yr[†]	8 d
Temporal pulse broadening ($\lambda = 30 \, {\rm cm}$)	1 ms	0.17 μs

[†] For the CGM case, the refractive timescales are quoted for two cases: (a) when the transverse velocity is $500 \, {\rm km \, s}^{-1}$ and (b) when the transverse velocity equals the speed of light (relevant for relativistically moving sources).

manifest on scales given by $\theta_{\rm diff} = r_{\rm diff}/D_{\rm l}$ on which individual speckles form. The ensemble of speckles form a scattering disc over the refractive scale given by $\theta_{\rm ap} = \theta_{\rm sc} D_{\rm ls}/D_{\rm s} = \lambda/(2\pi\theta_{\rm diff}) \, D_{\rm ls}/(D_{\rm s}D_{\rm l})$. Because $r_{\rm diff}$ evolves as $\lambda^{-6/5}$, the diffractive and refractive scales evolve as $\theta_{\rm diff} \propto \lambda^{-6/5}$ and $\theta_{\rm ap} \propto \lambda^{11/5}$. When the scattering is too weak to form speckles, the apparent size of a point-like source is set by the size of the first Fresnel zone given by $\theta_{\rm f}^2 = \lambda/(2\pi) \, D_{\rm ls}/(D_{\rm l}D_{\rm s})$. It is trivial to show that $\theta_{\rm f}^2 = \theta_{\rm diff}\theta_{\rm ap}$ and that all three angular scales are equal to one another at the transition wavelength: $\lambda_{\rm tran} = 2\pi r_{\rm diff}^2 \, D_{\rm s}/(D_{\rm l}D_{\rm ls})$. Below the transition wavelength, scattering is weak and manifests as weak flux-density modulation due to plasma density fluctuations that focus and de-focus the electromagnetic wavefront on
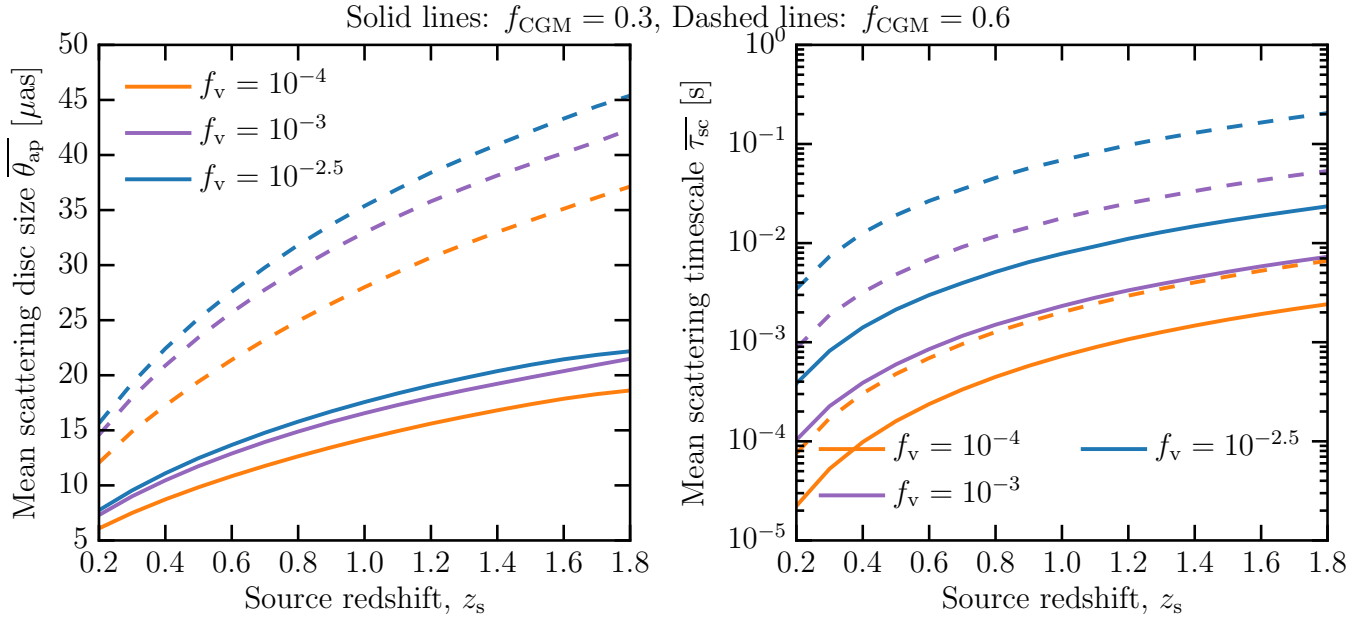
Figure 9. Mean angular (left) and temporal (right) broadening as a function of source redshift. Different lines show variation in cool gas volume fraction f_v and the fraction of cosmic baryons in the CGM, f_{CGM}. A photoionization background of $\Gamma(z) = 10^{-13}\,[(1+z)/1.2]^5\,\mathrm{s}^{-1}$ has been assumed.
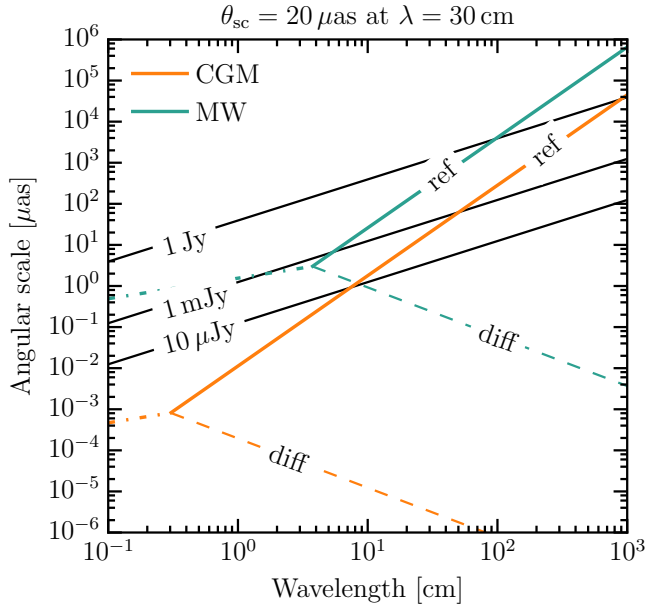
Figure 10. Plot showing the typical refractive and diffractive scales in the CGM (green lines) and Milky-way (orange lines) for a source at $z \gtrsim 1$. In either set of curves, the dot−dashed line ($\propto \lambda^{1/2}$) shows the weak scattering regime below the transition wavelength. In the strong scattering regime, the solid ($\propto \lambda^{11/5}$) and dashed ($\propto \lambda^{-6/5}$) curves show the refractive and diffractive scales respectively. The solid black lines ($\propto \lambda$) show the intrinsic angular size of an (incoherent) synchrotron source with a brightness temperature of 10^{12} K, and flux-density values given in the in-line labels. A length-scale of 1 Gpc has been assumed to convert all physical scales to angular scales.

the Fresnel scale. Above the transition wavelength, diffractive flux-density modulations results from fluctuations in the position and brightness of speckles that interfere at the observer, while refractive modulations result from focussing and de-focussing of the entire speckle ensemble. The above discussion applies to point-like sources. Refractive and diffractive scintillation of extended sources are rapidly 'washed out' as the intrinsic source size exceeds the diffractive and refractive scales respectively. Figure 10 and table 1 summarize the angular and time-scale of scintillation in the Galactic WIM at high Galactic latitudes and the corresponding CGM values for our fiducial test case.

4.2.2 Incoherent synchrotron sources

Let us first consider incoherent optically-thin synchrotron sources with a characteristic brightness temperature of 10^{12} K. Although the flux-density of such sources is strongly modulated by refractive effects for $\lambda \gtrsim 0.3$ cm, the time-scale over which these modulations manifest in light-curves is too large to be of practical interest. More importantly, even sources as faint as $10\,\mu$Jy are too large for refractive modulations to be observable at $\lambda \lesssim 10$ cm, whereas at $\lambda \gtrsim 10$ cm, the flux-density modulations are dominated by the Galactic WIM. Hence the influence of CGM scattering will be difficult to identify observationally using incoherent synchrotron sources. This conclusion also serves as an essential 'sanity-check' in that, our postulated existence of significant CGM scattering does not violate the large existing body of work on scintillation of incoherent synchrotron sources (active galactic nuclei and gamma-ray burst afterglow for e.g.) that only consider flux-modulations from Galactic scintillation.

There is however a narrow parameter range where CGM scattering may be discerned from Galactic scattering in weak

$< 10\,\mu$Jy-level sources. Consider the $3\,\mathrm{cm} \lesssim \lambda \lesssim 10\,\mathrm{cm}$ regime in Fig. 10. In the absence of CGM scattering, weak sources may be small enough to display diffractive scintillation in the Galaxy which could be observed as modulations in the radio spectrum of sources on scales of $\Delta\nu/\nu \approx (\nu/\nu_0)^{17/5}$ (Walker 1998, their §3.2.2). However, these scintillations will be quenched in the presence of angular broadening of the source in intervening CGM which could push the apparent source size above the Galactic diffractive scale. Given the large uncertainty in predictions for CGM scintillation parameters it is difficult to accurately predict where this wavelength window exists for a given sight-line. A targeted survey of sources along sight-lines at varying impact parameters (which would vary the transition frequency in Fig. 10) may be a fruitful avenue to explore. Assuming a characteristic coherence scale of $\Delta\nu \sim 1\,\mathrm{GHz}$, $\tau \sim 1\,\mathrm{hr}$ for Galactic diffractive scintillation, a system temperature of $30\,\mathrm{K}$, aperture efficiency of $60\,$per-cent, such an experiment would require a collecting area well in excess of $\sim 10^5\,\mathrm{m}^2$ which is barely within reach of existing radio telescopes.

We have also considered early radio emission from gamma-ray bursts (GRBs), which can have higher brightness temperatures at early times than blazars, owing to their ultrarelativistic velocities. They can therefore be brighter and easier to measure while still at small angular sizes, and are consequently observed to show interstellar scintillation in their first days at $\sim 5\,\mathrm{GHz}$ (Granot & van der Horst 2014). Before deceleration to Lorentz factor $\Gamma < 1/\theta_j$ (before the "jet break" for a jet of opening half-angle θ_j), the projected source angular size θ at (earth) time T after explosion of a GRB at redshift z is $\theta \sim 2cT\Gamma/D_M(z)$, where $D_M(z) = D_A(z)(1+z)$ is the proper motion distance, and $D_A(z)$ the angular diameter distance. The Blandford-McKee blast wave of the ultrarelativistic shock moving into a medium of uniform external density ρ_0 has radius $R \simeq 2cT\Gamma^2/(1+z)$ and explosion energy per unit solid angle $E/\Omega \simeq \rho_0 R^3 \Gamma^2 c^2$, which gives $\Gamma \simeq 9(E_{iso,53}/n_0)^{1/8}(T/[(1+z)\mathrm{day}])^{-3/8}$, where $E = 10^{53}\mathrm{erg}(\Omega/4\pi)E_{iso,53}$ and n_0 is the external density in cm^{-3} (Granot et al 2002, cf.). At $D_M(z=1) = 3.3\mathrm{Gpc}$, $\theta = [0.2, 1, 4]\,\mu\mathrm{as}$ at $T = [0.1, 1, 10]\,\mathrm{d}$. Thus at $\lambda < 4\mathrm{cm}$ (the transition wavelength below which Milky Way scintillation becomes unimportant), the GRB will be smaller than our fiducial scattering angle $\theta = 20\mu\mathrm{as}(\lambda/30\mathrm{cm})^{11/5} < 0.25\mu\mathrm{as}$ for less than 0.1 day. During this time, the scintillation timescale will be set by the rapidly expanding source, expanding across the refractive screen at a projected speed of $\sim \Gamma cD_l/D_s$. This is many times c for our cosmological lenses with $D_l \sim 0.5D_s$ (but less than $1\,\mathrm{km\,s}^{-1}$ for Milky Way interstellar plasma at $D_l \sim 100\mathrm{pc}$, so Milky Way scintillation timescales are dominated by gas motions in the Milky Way, not the apparent source expansion). The refractive scintillation timescale is thus the same as the timescale for the source to expand to a size larger than the refractive scale —i.e., the source will have only about 1 speckle before becoming too large to display refractive scintillation. This would be difficult to convincingly detect in a GRB.

We thus turn to the most promising class of sources.

4.2.3   Coherent sources

Fast radio bursts (FRB; Lorimer et al. 2007) are the only known class of coherent emitters at cosmic distances of interest to CGM scintillation. Extragalactic mega-masers are known to scintillate due to the Galactic turbulence (Argon et al. 1994). However, even if they are compact enough to show diffractive scintillation in intervening CGM, the interpretation is clouded by the possibility of intrinsic variability (see e.g. Greenhill et al. 1997), and we will not consider them here. FRBs are $\lesssim 1\,\mathrm{ms}$ duration bright ($\sim 1\,\mathrm{Jy}$) radio bursts of extragalactic origin. At least one FRB is known to repeat (Spitler et al. 2016) which is the only FRB to have been securely localized, and resides in a galaxy with redshift $z_s = 0.193$ (Chatterjee et al. 2017; Tendulkar et al. 2017). However, if most of the observed plasma dispersion is apportioned to the intergalactic medium, then the known populations of FRBs with dispersion measures DM $\sim 500 - 2000\,\mathrm{pc\,cm}^{-3}$ (Petroff et al. 2016; Ravi 2017) originate at redshifts of $z \sim 0.5 - 2$. In this redshift range, the spectra of quasars show absorption systems, e.g. in Mg II, CIV, Lyman limit systems produced in the halos of one or more intervening galaxies(Steidel et al. 1988, 1994; Mathes et al. 2017). Thus signals from cosmological FRBs must also be passing through the cool ionized clumps in the CGM of galaxies.

Based on their $\sim \mathrm{ms}$ duration, FRBs should projected an angular size of $\sim 10^{-6}\,\mu\mathrm{as}$ at $D_s \sim 1\,\mathrm{Gpc}$, even if the emission region travels with apparent superluminal speed with relativistic $\gamma \sim 10^3$. Hence FRBs must display the effects of diffractive (and refractive) scintillation in both intervening CGM and the Galactic WIM. The characteristic pulse broadening time-scale in the CGM of $\gtrsim 1\,\mathrm{ms}$ should also be easily distinguishable from the $\lesssim 0.1\,\mu\mathrm{s}$ of broadening expected in the Galactic WIM at high latitudes, and a presumably similar amount from the FRB host galaxy. Some FRBs may also originate in dense star-forming regions which may contribute significantly to temporal broadening. CGM scattering can however be distinguished in a population of localized FRBs in two ways. (a) One can attempt a statistical detection of an FRB temporal broadening v/s redshift relationship and constrain the amount of cool gas in the CGM fog (via Fig. 9. (b) The variation of temporal broadening with halo mass and impact parameter can be measured (with significant investment of time on optical spectrographs, comparable to that invested in quasar studies, e.g.(Steidel et al. 1994)) and CGM scattering constrained via equation 24 and 5. These appear to be the most promising avenues to directly constrain the fine sub-parsec scale properties of cool gas in the CGM.

With the current absence of a sample of well localized FRBs, we can only make a heuristic comparison between our predictions and data. If a large fraction of the observed FRBs at $\lambda = 30\,\mathrm{cm}$ are indeed at $z \sim 1$ as they dispersion measures suggest (Petroff et al. 2016), then based on Fig. 8, the most extreme models with $f_V \gtrsim 10^{-3}$ and $f_{\mathrm{CGM}} \gtrsim 0.6$ are disfavored. The more moderate models such as $(f_{\mathrm{CGM}} = 0.3, f_V = 10^{-4})$ or $(f_{\mathrm{CGM}} = 0.6, f_V = 10^{-4})$ are broadly consistent with the $\sim$ms scale scattering seen in some FRBs if they are at $z \sim 1$. The same models also predict $> 1\,\mathrm{s}$ of scattering at frequencies below $\sim 200\,\mathrm{MHz}$, making them difficult to detect. This is a plausible expla-

nation for the current non-detection of FRBs at such low frequencies (Chawla et al. 2017; Tingay et al. 2015; Karastergiou et al. 2015).

4.3 Summary

In addition to the hot 10^6 K halo gas, quasar absorption spectroscopy and fluorescent Lyα imaging have detected large amounts of cool 10^4 K gas in the CGM of $\gtrsim 10^{12}\,M_\odot$ haloes. This was not predicted in canonical galaxy assembly models, but has been accounted for in recent simulations of cooling instabilities that drive the formation of numerous sub-pc size cloudlets of cool gas. The tiny size of these cloudlets make their spectroscopic or imaging-based detection (and even study via simulations) difficult. We have shown that the pc-scale 'granularity' imparted by the small cloudlet size results in a large increase in their radio wave scattering strength. The resulting temporal broadening at $\lambda = 30$ cm of $\sim 10^{-1} - 10$ ms (depending on cool gas volume fraction and fraction of baryons in CGM) far exceeds that expected from the Galactic WIM. This makes their study feasible with fast radio bursts. Identification of our predicted associated temporal broadening in FRBs could revolutionized study of small-scale structure of the CGM in much the same way that pulsars revolutionized our understanding of sub-au scale structure in the Galactic WIM. We have computed the scattering properties of individual haloes (equations 21 to 24) as function of halo parameters and redshift, as well as ensemble scattering properties through sight-lines in the Universe (9). The imprint of CGM scattering on the angular size and scintillation of faint compact radio sources may be difficult to discriminate from scattering in the Galactic WIM. A population of well localized FRBs however, will provide a much more promising avenue to measure the sub-pc scale structure of the CGM. Such a measurement will however have to discriminate between scattering in intervening CGM and other plausible scattering sites such as the circum-burst medium.

We end by noting that while we have demonstrated the observable scattering effects of cool gas clouds, the precise CGM model considered here is likely simplistic. For instance, McCourt et al. (2018) considered equilibrium cooling rates for collisionally ionized solar-metallicity gas that is optically thin. These and other assumptions (see e.g. §4.1 of McCourt et al. 2018) likely break-down at least in some parameter ranges of redshift, halo mass and galaxy type. Our *method* to compute CGM scattering from small-scale cool-gas clouds presented here can however be readily adapted to future refinement of CGM cool-gas models.

REFERENCES

Anderson, M. E., & Bregman, J. N. 2010, ApJ, 714, 320
Argon, A. L., Greenhill, L. J., Moran, J. M., et al. 1994, ApJ, 422, 586
Armstrong, J. W., Rickett, B. J., & Spangler, S. R. 1995, ApJ, 443, 209
Binney, J. 1977, ApJ, 215, 483
Blandford, R., & Narayan, R. 1985, MNRAS, 213, 591
Borisova, E., Cantalupo, S., Lilly, S. J., et al. 2016, ApJ, 831, 39
Cantalupo, S., Arrigoni-Battaia, F., Prochaska, J. X., Hennawi, J. F., & Madau, P. 2014, Nature, 506, 63
Chatterjee, S., Law, C. J., Wharton, R. S., et al. 2017, Nature, 541, 58
Chawla, P., Kaspi, V. M., Josephy, A., et al. 2017, ApJ, 844, 140
Dunkley, J., Komatsu, E., Nolta, M. R., et al. 2009, ApJS, 180, 306
Faucher-Giguère, C.-A., Feldmann, R., Quataert, E., et al. 2016, MNRAS, 461, L32
Field, G. B. 1965, ApJ, 142, 531
Fielding, D., Quataert, E., McCourt, M., & Thompson, T. A. 2017, MNRAS, 466, 3810
Gaikwad, P., Khaire, V., Choudhury, T. R., & Srianand, R. 2017, MNRAS, 466, 838
Granot, J., Panaitescu, A., Kumar, P. & Woosley, S. E. 2002, ApJ, 570, L61
Granot, J., van der Horst, A. J. 2014, Publ. Astron. Soc. Australia, 31, e008
Goodman, J., & Narayan, R. 1985, MNRAS, 214, 519
Greenhill, L. J., Ellingsen, S. P., Norris, R. P., et al. 1997, ApJ, 474, L103
Hennawi, J. F., Prochaska, J. X., Cantalupo, S., & Arrigoni-Battaia, F. 2015, Science, 348, 779
Jeans, J. H. 1902, Philosophical Transactions of the Royal Society of London Series A, 199, 1
Ji, S., Oh, S. P., & McCourt, M. 2017, arXiv:1710.00822
Karastergiou, A., Chennamangalam, J., Armour, W., et al. 2015, MNRAS, 452, 1254
Kereš, D., Katz, N., Weinberg, D. H., & Davé, R. 2005, MNRAS, 363, 2
Lau, M. W., Prochaska, J. X., & Hennawi, J. F. 2016, ApJS, 226, 25
Lorimer, D. R., Bailes, M., McLaughlin, M. A., Narkevic, D. J., & Crawford, F. 2007, Science, 318, 777
Manchester, R. N., Hobbs, G. B., Teoh, A., & Hobbs, M. 2005, AJ, 129, 1993
Mathes, N. L., Churchill, C. W. & Murphy, M. T. 2017, arXiv:1701.05624
McCourt, M., Oh, S. P., O'Leary, R. M., & Madigan, A.-M. 2018, MNRAS, 473, 5407
Murray, S. G., Power, C., & Robotham, A. S. G. 2013, Astronomy and Computing, 3, 23
Petroff, E., Barr, E. D., Jameson, A., et al. 2016, Publ. Astron. Soc. Australia, 33, e045
Planck Collaboration, Ade, P. A. R., Aghanim, N., et al. 2016, A&A, 594, A13
Prochaska, J. X., & Hennawi, J. F. 2009, ApJ, 690, 1558
Putman, M. E., Peek, J. E. G., & Joung, M. R. 2012, ARA&A, 50, 491
Ravi, V. 2017, arXiv:1710.08026
Rees, M. J., & Ostriker, J. P. 1977, MNRAS, 179, 541
Rickett, B. J., Coles, W. A., & Bourgois, G. 1984, A&A, 134, 390
Rickett, B. J. 1990, ARA&A, 28, 561
Rudie, G. C., Steidel, C. C., Trainor, R. F., et al. 2012, ApJ750, 67
Silk, J. 1977, ApJ, 211, 638
Spitler, L. G., Scholz, P., Hessels, J. W. T., et al. 2016, Nature, 531, 202

Steidel, C. S., Sargent, W. L. W. & Boksenberg, A. 1988, ApJ,
    333, L5
Steidel, C. S., Dickinson, M. & Persson, S. E. 1994, ApJ, 437, L75
Stocke, J. T., Keeney, B. A., Danforth, C. W., et al. 2013, ApJ,
    763, 148
Tendulkar, S. P., Bassa, C. G., Cordes, J. M., et al. 2017, ApJ,
    834, L7
Tingay, S. J., Trott, C. M., Wayth, R. B., et al. 2015, AJ, 150,
    199
Tumlinson, J., Peeples, M. S., & Werk, J. K. 2017, ARA&A, 55,
    389
Turner, M. L., Schaye, J., Steidel, C. C., Rudie, G. C. & Strom,
    A. L. 2014, MNRAS, 445, 794
Walker, M. A. 1998, MNRAS, 294, 307
Werk, J. K., Prochaska, J. X., Tumlinson, J., et al. 2014, ApJ,
    792, 8
White, S. D. M., & Rees, M. J. 1978, MNRAS, 183, 341

Table 1. Glossary of symbols and their implied meaning

Symbol	Meaning
λ	Observed wavelength
λ_{30}	λ in units of $30\,\mathrm{cm}$
N_e	Electron column density through a single cloudlet
$N_{e,17}$	N_e in units of $10^{17}\,\mathrm{cm}^{-2}$
r_c	Radius of a single cloudlet
f_a	Average number of cloudlets intercepted
f_CGM	Fraction of baryons in CGM (halo mass and redshift independent)
r_diff	Diffractive scale of plasma inhomogeneities
θ_sc	Characteristic wave scattering angle
$\Delta\tau$	Characteristic pulse broadening timescale
r_{200}	Radius at which halo density is $200\times$ critical density
M_{200}	Mass enclosed within r_{200}
M_{12}	M_{200} in units of $10^{12}\,M_\odot$
b	Impact parameter
b_{200}	Impact parameter in units of r_{200}
b_c	Radius below which cloudlets self-shield against photoionization
$b_\mathrm{c,200}$	b_c in units of r_{200}
P_{200}	Gas pressure at r_{200}
T, T_4	Gas temperature in units of Kelvin and 10^4 Kelvin respectively
α	Power-law index for variation of gas pressure with radius
β	Power-law index for variation of cool-gas volume fraction with radius
$D_\phi(r)$	Phase structure function at transverse separation r
D_l	Observer$-$Lens angular diameter distance
D_s	Observer$-$Source angular diameter distance
D_{ls}	Lens$-$Source angular diameter distance
r_e	Classical electron radius $\approx 2.81794 \times 10^{-13}$ cm.

APPENDIX A: PHASE STRUCTURE FUNCTION OF A CLOUDLET ENSEMBLE

Let the two dimensional impact parameters vector be $\boldsymbol{b} = [b_x, b_y]$, and let us use the notation $|\boldsymbol{x}| \equiv x$ for spatial vectors. If there are f_a cloudlets intercepted by a ray, then the number of cloudlets intercepted with impact parameters within an interval $\mathrm{d}b_x\,\mathrm{d}d_y$ around $[b_x, b_y]$ is a Poisson random variable with mean

$$\left\langle \frac{\partial^2 N(b_x, b_y)}{\partial b_x\, \partial b_y} \right\rangle = \frac{f_\mathrm{a}}{\pi r_\mathrm{c}^2}. \tag{A1}$$

Let $f(\boldsymbol{b}) \in [0, 1)$ be the fractional path-length through a cloudlet. Because $\lambda r_e N_e$ is the maximal phase through a cloudlet, the phase inserted into a ray at impact parameter $\boldsymbol{b}$ is therefore $\lambda r_e N_e f(\boldsymbol{b})$. With these definitions, the phase structure function at transverse separation Δr can be written as the ensemble average:

$$D_\phi(\Delta r) = \left\langle \left(\int \mathrm{d}b_x \int \mathrm{d}b_y\, \frac{\partial^2 N(b_x, b_y)}{\partial b_x\, \partial b_y} \lambda r_e N_e \left[f(\boldsymbol{b}) - f(\boldsymbol{b} + \boldsymbol{\Delta r}) \right] \right)^2 \right\rangle. \tag{A2}$$

We now bring in the assumption that cloudlets are randomly distributed. The random variable $\partial^2 N(b_x, b_y)/\partial b_x\, \partial b_y$ therefore has the properties

$$\left\langle \frac{\mathrm{d}^2 N(b_x, b_y)}{\mathrm{d}b_x\, \mathrm{d}b_y} \frac{\mathrm{d}^2 N(b_x', b_y')}{\mathrm{d}b_x'\, \mathrm{d}b_y'} \right\rangle = \frac{2f_\mathrm{a}}{\pi r_\mathrm{c}^2} \text{ if } b_x = x_x', \, b_y = b_y'$$
$$= 0 \text{ otherwise} \tag{A3}$$

With this, the structure function reduces to

$$D_\phi(\Delta r) = \lambda^2 r_e^2 N_e^2\, 2 f_\mathrm{a} \times \frac{\int \mathrm{d}b_x\, \mathrm{d}b_y\, \left[f(\boldsymbol{b}) - f(\boldsymbol{b} + \Delta r) \right]^2}{\pi r_\mathrm{c}^2}. \tag{A4}$$

The first factor is the variance of the phase accumulated by a ray propagating through the cloudlet ensemble. The second factor, defined as the function $\Psi(.)$ in §3, only depends on the internal structure of the cloudlets. For axially symmetric cloudlets, it is only a function of $\Delta r/r_\mathrm{c}$. It increases from 0 for $\Delta r = 0$ and saturates at 1 for $\Delta r \geq r_\mathrm{c}$

APPENDIX B: PHOTOIONIZATION BALANCE IN THE GALACTIC FOG

We make the following simplifying assumption in our computation of the photoionization balance: (a) all neutral hydrogen atoms are in the ground state, (b) photons emitted during direct recombinations to the ground state are all reabsorbed

'close by' in the halo (so called on-the-spot approximation), (c) only photons close to $\nu_0 = 3.3 \times 10^{15}$ Hz participate in the ionization balance (d) the free-electrons have a Maxwellian distribution owing to their large elastic scattering cross-section ($\sim 10^{-13}$ cm^{-2}).

Let $J_{\nu_0}(r)$ be the number of photons at frequency ν_0 per unit area, per unit solid angle, per unit frequency per unit time present in the halo at radial distance r (i.e. $\mathcal{I}_{\nu_0} = J_{\nu_0}/(h\nu_0)$). The boundary condition for photoionization equilibrium is set by the measured/modelled UV photon field in the IGM, which is typically specified as an isotropic photoionization rate:

$$\Gamma(\mathrm{IGM}) = 4\pi \, J_{\nu_0}(\mathrm{IGM}) \, a_0 \tag{B1}$$

where $a_0 \approx 6.3 \times 10^{-18}$ cm^{-2}. Gaikwad et al. (2017) determined a photoionization rate of $\Gamma(\mathrm{IGM}) = 10^{-13} \left[(1+z)/1.2\right]^5$. This gives the boundary condition of

$$4\pi a_0 J_{\nu_0} = 10^{-13} \left[(1+z)/1.2\right]^5 \tag{B2}$$

At any location r in the halo, if $\zeta(r)$ is the neutral fraction, then photionization balance is enforced via

$$\frac{[1 - \zeta(r)]^2}{\zeta(r)} = \frac{\Gamma(r)}{n(r)\alpha_{\mathrm{B}}} \tag{B3}$$

where $\alpha_B = 2.6 \times 10^{-13}$ cm^{-3} s^{-1} at $T = 10^4$ K is the effective recombination coefficient for the on-the-spot approximation, and $n(r)$ is the total density.

$\Gamma(r)$ is evaluated by the equation of radiative transfer. Recombinations to levels other than the ground state do not contribute photons for ionization, and photons from recombinations to the ground state have been accounted for in α_{B}. This simplifies the equation of radiative transfer substantially (no source term).

$$\Gamma(r) = 2\pi \int_0^\pi \mathrm{d}\theta \sin\theta \, J_{\nu_0}(\mathrm{IGM}) \, \exp^{-\tau(r,\theta)} \tag{B4}$$

where $\tau(r,\theta)$ is the optical depth to ionizing photons arriving at radius r from the IGM, at a polar angle θ:

$$\tau(r,\theta) = a_0 \int_0^\infty \mathrm{d}x \, n(x)\zeta(x) \, f_{\mathrm{v}}(x) \tag{B5}$$

where the integrand is just the column density of neutral atoms along the ray, and x is the affine parameter along the ray. The above equation will need to be evaluated numerically for a spherical geometry that we are considering here (unlike the plane-parallel approximation that is usually employed).

Taken together, we are now tasked with solving the following integral equation in $\zeta(r)$

$$\frac{[1 - \zeta(r)]^2}{\zeta(r)} = \frac{\Gamma(\mathrm{IGM})}{2\alpha_{\mathrm{B}}n(r)} \int_0^\pi \mathrm{d}\theta \, \sin\theta \, \exp\left[-a_0 \int_0^\infty \mathrm{d}x \, n(x)\zeta(x)f_{\mathrm{v}}(x)\right] \tag{B6}$$

Any given set of halo mass and redshift completely specify $n(x)$, $r_{\mathrm{c}}(x)$, $f_{\mathrm{v}}(x)$, and $\Gamma(\mathrm{IGM})$. This allows us to solve for $\zeta(x)$ recursively via

$$\frac{[1 - \zeta_{i+1}(r)]^2}{\zeta_{i+1}(r)} = \frac{\Gamma(\mathrm{IGM})}{2\alpha_{\mathrm{B}}n(r)} \int_0^\pi \mathrm{d}\theta \, \sin\theta \, \exp\left[-a_0 \int_0^\infty \mathrm{d}x \, n(x)\zeta_i(x)f_{\mathrm{v}}(x)\right] \tag{B7}$$

We choose an initial value by setting the optical depth term to unity:

$$\frac{[1 - \zeta_0(r)]^2}{\zeta_0(r)} = \frac{\Gamma(\mathrm{IGM})}{\alpha_{\mathrm{B}}n(r)} \tag{B8}$$
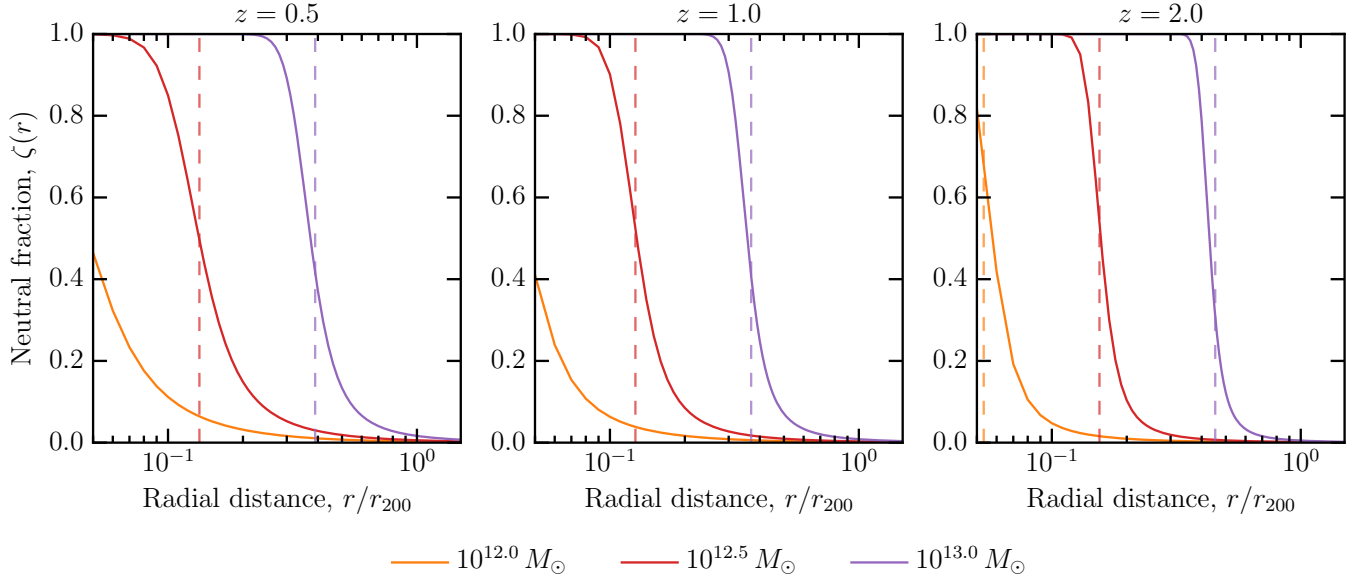
An approximate location of the ionization front can be found by assuming (i) a radiation field given by $\Gamma(\mathrm{IGM})$ throughout the halo to compute the neutral fraction in each cloud, and (ii) computing the radial depth at which the ensuing neutral fraction yields a column density of a_0^{-1}. Because individual clouds at the outskirts of the halo are only partially neutral, we have $\zeta(r) \approx n(r)\alpha_{\mathrm{B}}/\Gamma(\mathrm{IGM})$. Setting the neutral column density integrated from the halo edge, $r_{\mathrm{shock}} = 1.5 \, r_{200}$ to the self-shielding radius r_{ss} in units of r_{200}, to a_0^{-1}, we get

$$a_0\alpha_{\mathrm{B}}/\Gamma(\mathrm{IGM})r_{200} \int_{r_{\mathrm{ss}}}^{1.5} \mathrm{d}(r/r_{200}) \, n^2(r/r_{200})f_{\mathrm{v}}(r/r_{200}) = 1 \tag{B9}$$

We can let the upper limit of integration to recede to infinity without significant loss of accuracy, substitute for the radial scaling of density and volume fraction from §2, and get an approximate expression for the self-shielding radius in units of r_{200}

$$r_{\mathrm{ss}} \approx 0.11 \left(\frac{f_{\mathrm{v}}}{10^{-4}}\right)^{0.56} \left(\frac{f_{\mathrm{CGM}}}{0.3}\right)^{1.11} M_{12}^{0.93} \frac{h^{2.59}(z)}{(1+z)^{2.78}}. \tag{B10}$$

We have adjusted the numerical constant with a factor of order unity to match r_{ss} to the radius at which $\zeta = 0.5$ (within ~ 10 per-cent) for mass and redshift ranges of interest, in the neutral profile determined from the full radiative transfer as per equation B7. Figure B1 shows the neutral fraction profile evaluated using equation B7 and the approximation for r_{ss} given above.

Figure B1. Neutral fraction profile, $\zeta(r)$, computed using full radiative transfer of the IGM UV field from equation B7 for different redshifts and halo mass (halo properties defined in §2). The dashed lines show the location of the ionization front as approximated by equation B10.